Direct Observation of Ultrafast Hydrogen Bond Strengthening in Liquid Water

Jie Yang[1,2,11]*, Riccardo Dettori[3], J. Pedro F. Nunes[4], Nanna H. List[1,2,5], Elisa Biasin[1,2], Martin Centurion[4], Zhijiang Chen[1], Amy A. Cordones[2], Daniel P. Deponte[1], Tony F. Heinz[2,6], Michael E. Kozina[1,2], Kathryn Ledbetter[2,7], Ming-Fu Lin[1], Aaron M. Lindenberg[2,8,9], Mianzhen Mo[1], Anders Nilsson[10], Xiaozhe Shen[1], Thomas J. A. Wolf[1,2], Davide Donadio[3]*, Kelly J. Gaffney[2]*, Todd J. Martinez[1,2,5]*, Xijie Wang[1]*

[1]SLAC National Accelerator Laboratory, Menlo Park, CA, USA.
[2]Stanford PULSE Institute, SLAC National Accelerator Laboratory, Menlo Park, CA, USA.
[3]Department of Chemistry, University of California-Davis, Davis, CA, USA.
[4]Department of Physics, University of Nebraska-Lincoln, Lincoln, NE, USA.
[5]Department of Chemistry, Stanford University, Stanford, CA, USA.
[6]Department of Applied Physics, Stanford University, Stanford, CA, USA.
[7]Department of Physics, Stanford University, Stanford, CA, USA.
[8]Department of Materials Science and Engineering, Stanford University, Stanford, CA, USA.
[9]Stanford Institute for Materials and Energy Sciences, SLAC National Accelerator Laboratory, Menlo Park, CA, USA.
[10]Department of Physics, AlbaNova University Center, Stockholm University, Stockholm, Sweden.
[11]Present address: Center of Basic Molecular Science, Department of Chemistry, Tsinghua University, Beijing, China
*email: jieyang1@tsinghua.edu.cn; ddonadio@ucdavis.edu; kgaffney@slac.stanford.edu; todd.martinez@stanford.edu; wangxj@slac.stanford.edu.

Water is one of the most important, yet least understood, liquids in nature. Many anomalous properties of liquid water originate from its well-connected hydrogen bond network[1], including unusually efficient vibrational energy redistribution and relaxation[2]. An accurate description of the ultrafast vibrational motion of water molecules is essential for understanding the nature of hydrogen bonds and many solution-phase chemical reactions. Most existing knowledge of vibrational relaxation in water is built upon ultrafast spectroscopy experiments[2-7]. However, these experiments cannot directly resolve the motion of the atomic positions and require difficult translation of spectral dynamics into hydrogen bond dynamics. Here we measured the ultrafast structural response to the excitation of the OH stretching vibration in liquid water with femtosecond temporal and atomic spatial resolution using liquid ultrafast electron scattering. We observed a transient hydrogen bond contraction of roughly 0.04 Å on a timescale of 80 femtoseconds, followed by a thermalization on a timescale of ~1 picosecond. Molecular dynamics simulations reveal the need to treat the distribution of the shared proton in the hydrogen bond quantum mechanically to capture the structural dynamics on the femtosecond timescales. Our experiment and simulations unveiled the intermolecular character of the water vibration preceding the relaxation of the OH stretch.

The vibrational spectroscopy of water has critically contributed to our understanding of the dynamics of hydrogen bond (HB) reorganization and energy redistribution in liquid water. It is

established that the vibrational spectrum of water has both intra- and intermolecular character[4] and needs to be described in terms of collective excitations[8], but the spectrum-to-structure interpretation has proven challenging due to many complications, including the strong anharmonic coupling among intra- and intermolecular vibrational modes[8]. A complete unveiling of the intermolecular dynamics of water requires direct time- and structure-resolved measurements. Neutron and X-ray scattering are routinely used to measure the equilibrium atomic structure of liquid water in different environments[9,10], femtosecond (fs) X-ray pulses generated from X-ray free-electron-lasers (XFELs) have been used to study ultrafast heating[11,12] and cage effects[13] in water, and inelastic neutron scattering has provided great insights on both intra- and intermolecular vibrational dynamics in water[9]. In addition, XFELs have allowed the study of femtosecond structural dynamics of molecules in solution[14,15]. Nevertheless, neither X-ray nor neutron scattering has been exploited to study the ultrafast vibrational relaxation of water in a pump-probe scheme.

Recently, liquid ultrafast electron scattering (LUES) was enabled by the combination of an ultrathin liquid sheet jet with a mega-electron-volt (MeV) electron beam[16]. The experimental setup is schematically shown in Fig. 1a. The sample is delivered through a gas-accelerated liquid sheet jet[17] with a thickness of ~100 nm. We used a ~3315 cm^{-1} IR pulse to excite the OH stretching vibration in the sample and probed it with a 3.7 MeV electron pulse. The scattering pattern in the range of $0.2<Q<11.8$ $Å^{-1}$ was recorded on an electron detector. Approximately 5% of the probed molecules were excited. The instrument response function (IRF) of the system was roughly 200 fs full-width-at-half-maximum (FWHM) (Methods). The static scattering intensity $I^{exp}(Q)$ is shown in Fig. 1b along with a simulated $I^{sim}(Q)$ and its elastic and inelastic component (Methods), where Q is the momentum transfer between the scattered and the incident MeV electrons. The inelastic component is a smooth curve that dominates over small Q, and the structure in the elastic component encodes the atomic structure of water.

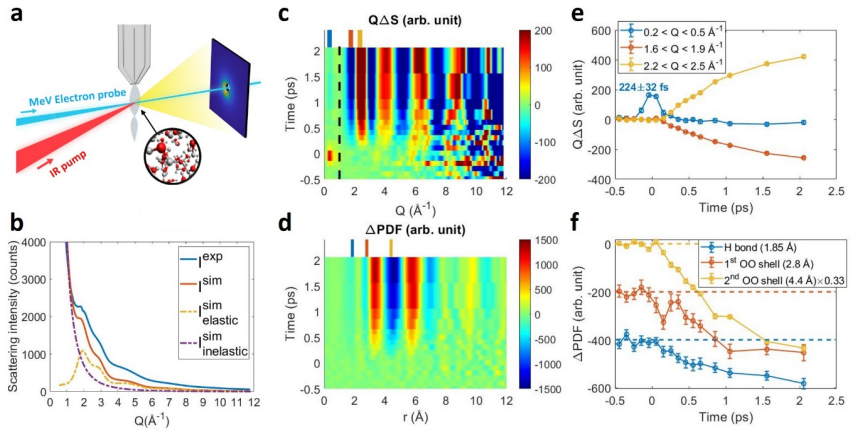

Fig. 1 | Experiment overview. a, A schematic of the experimental setup. The pump IR laser (red) and probe electron pulse (blue) are introduced to the interaction point with a 30-degree

angle. The ~100 nm water sample is delivered through a gas-accelerated sheet jet. The scattering patterns are recorded on a phosphor screen-based detector. **b,** Experimental static scattering (blue solid) plotted together with simulated static scattering (red solid) and its elastic (yellow dashed) and inelastic (purple dashed) components. **c**, Experimental difference scattering curve $Q\Delta S$ displayed in false color map. The black dashed line represents Q = 1 Å^{-1}, which roughly separates the inelastic (Q<1 Å^{-1}) and elastic (Q>1 Å^{-1}) contributions. The three colored bands on top show the Q ranges over which the data in part **e** are integrated. **d**, Experimental ΔPDF displayed in false color map, calculated using 1<Q<11.8 Å^{-1}. The three colored bands on top show the r ranges over which the data in part **f** are integrated. **e**, $Q\Delta S$ at three different Q ranges shown in the legend. **f**, ΔPDF at three important distances shown in the figure legend. Dashed lines show the baseline for each curve. The blue and orange curves are shifted vertically for visibility. Error bars in parts **e** and **f** represent standard error of the mean (SEM) of 60 independent measurements.

Similar to previous time-resolved X-ray scattering studies[14], we use difference scattering curves $Q\Delta S$ (Methods) to show the change in the scattering pattern as a function of pump-probe delay, as depicted in Fig. 1c. The time evolution of three transient features is plotted in Fig. 1e. Most features at Q > 1 Å^{-1} have a slow picosecond (ps) turn on, but the low-Q (0.2 < Q < 0.5 Å^{-1}) feature is short-lived with a time constant of 224±32 fs (mean±1SE from Gaussian fit). We attribute the appearance and disappearance of this feature to the change in inelastic scattering amplitude upon excitation and relaxation of the OH stretching mode. This interpretation is supported by an *ab initio* electron scattering simulation shown in Extended Data Fig. 1a. In this work, time zero is determined by the peak of this transient signal (Fig. 1e).

The difference pair distribution function (ΔPDF), calculated through a Fourier-sine transform of the $Q\Delta S$ curve[18] (see Methods), is shown in Fig. 1d. The strongest features in the ΔPDF are the broadening of the 2nd OO coordination shell, indicated by a bleaching band of the original 2nd OO shell location (~4.4 Å) and the emergence of two strong positive bands next to it. These features agree well with the ΔPDF of equilibrium water under different temperatures measured in a previous X-ray scattering experiment.[19] The time evolution of the ΔPDF intensity at three major short-range distances— the initial HB OH at ~1.85 Å, the 1st OO shell at ~2.8 Å and the 2nd OO shell at ~4.4 Å—are shown in Fig. 1f. At all three distances, the ΔPDF intensity becomes negative after time zero, indicating the loss of the intermolecular order present prior to vibrational excitation. The ~1 ps relaxation timescale was observed in many previous ultrafast spectroscopy experiments in pure water and was ascribed to the overall thermalization of the sample.[2-6] This thermalization has also been routinely observed in the case of photoexcited solutes in aqueous solution[20]. However, the ΔPDF intensity assigned to the 1st OO shell shows a non-monotonic time dependence in the first ~500 fs, which resembles the underdamped oscillation observed in a previous vibrational echo measurement[6]. This feature is a result of the initial structural response before the vibrational energy relaxation. In the rest of the manuscript, we will first focus on the 1st shell HB dynamics in Fig. 2, then present the dynamics of hydrogen atoms in the 1st coordination shell in Fig. 3, and finally examine the thermalization dynamics in Fig. 4.

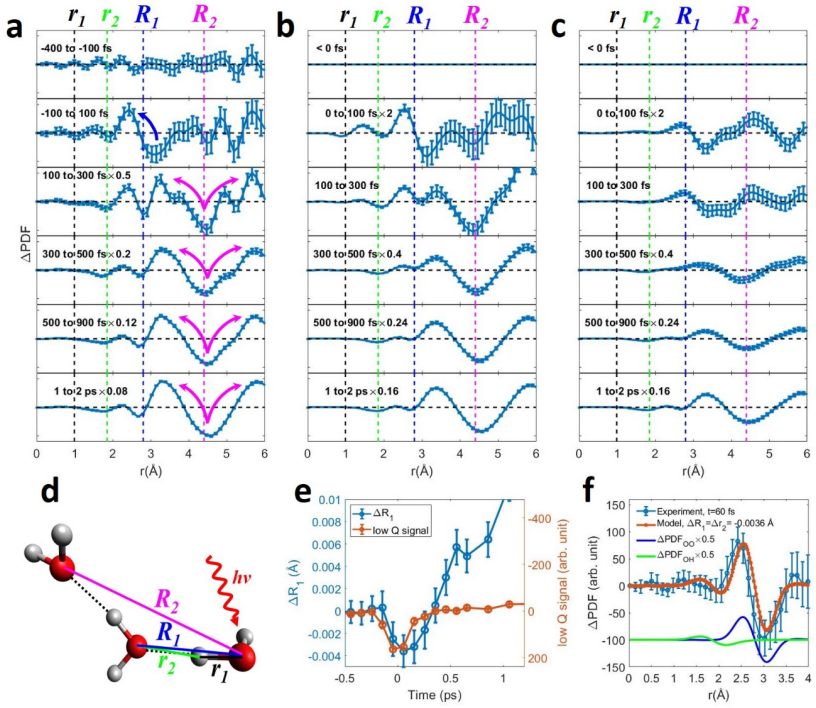

Fig. 2 | Transient HB strengthening. a-c, Experimental (**a**), simulated with quantum excitation (**b**), and simulated with classical excitation (**c**) ΔPDF for six selected time windows. Vertical dashed lines indicate the initial position of four distances (color code see part **d**). The vertical scale is the same for all sub-panels. Horizontal dashed lines are the baseline for each curve. The rows 2-6 in part **a** are scaled by 1, 0.5, 0.2, 0.12 and 0.08, and in part **b-c** are scaled by 2, 1, 0.4, 0.24 and 0.16, respectively. Colored arrows denote important atomic motions (see text). **d**, A ball-and-stick model showing four important distances. The color codes of the four important atom pairs are: black for covalent OH bonded r_1, green for hydrogen bonded r_2, blue for 1st OO shell R_1, and magenta for 2nd OO shell R_2. The wavy arrow represents the photoexcitation. **e,** The fitted 1st OO contraction from experimental data (blue symbols, left axis) and the low-Q signal (orange symbols, right axis). **f,** The experimental ΔPDF at 60 fs and its best fit (see text). The underlying ΔPDF for OO and OH pairs are plotted with a vertical shift for visibility. Symbols represent measurement and lines represent a Gaussian fitting. Error bars representing the SEM of 60 independent measurements (**a**, blue curve in **f,** orange curve in **e**), the SEM of 200 independent simulations (**b**, **c**), or the standard error from the fit (blue curve in **e**).

The experimental ΔPDFs over six selected time windows are displayed in Fig. 2a. In this manuscript, we use lower case letter "*r*" to represent OH distances and upper case letter "*R*" to

represent OO distances, see Fig. 2d. Starting at 100-300 fs, the broadening of R_2 becomes the strongest signal (magenta arrows), marking the beginning of the ~1 ps heating process. For -100 to 100 fs, when the R_2 signal is still nearly absent, a strong contraction of R_1 is observed (blue arrow), indicating a transient strengthening of the HB. We extract the HB length change as a function of delay time using a simple single-parameter model: we assume that all of the R_1 and r_2 pairs expand or contract by the same amount ΔR_1 as a result of the motion of the 1st shell oxygen atom, with no change in any other atom pair distances (Methods). The fitting is applied for the ΔPDF signal between 1.5 and 3 Å to focus on the first coordination shell dynamics. The fitting results (blue curve in Fig. 2e) show a fast mean R_1 contraction of all OO distances with a maximum value of 0.0036±0.0014 Å (mean±1SE from fit), that disappears as the v_{OH}=1 population decays. This decay initiates a slower (~1 ps) R_1 expansion. Figure 2f shows the experimental and fitted ΔPDF at the maximum contraction (i.e. at 60 fs). Most features in the ΔPDF are captured by this simple 1-parameter model, except a deviation around the zero-crossing at 2.7 Å that will be discussed in Fig. 3. The time delay between the photoexcitation and the R_1 contraction is 81±51 fs (SE from Gaussian fit), a value roughly equal to the half period of the HB stretching coordinate, as expected for the underdamped contraction of the HB.

The early R_1 contraction reflects the dynamics in the excited-unexcited OO pairs (one oxygen atom in the pair is from an excited molecule, and the other is from a neighboring unexcited molecule), which only accounts for 10% of atom pair population when the excitation fraction is 5%. Using 10% as a scaling factor, we obtain the averaged R_1 contraction to be 0.036±0.014 Å for excited-unexcited pairs.

We performed extensive nonequilibrium molecular dynamics (MD) simulations using a neural network potential trained on *ab initio* MD simulations[21] (Methods). The excitation process was modeled in two different ways: classical excitation with a hot-spot thermostat based on the generalized Langevin equation[22,23] for 100 fs; instantaneous quantum excitation using the pure state v_{OH}=1 Wigner phase-space sampling based on the refined Lippincott–Schroeder model[5], thereby accounting for the phase-space configurations of the excited quantum OH stretch vibrational state in a hydrogen bonded system (Extended Data Fig. 2). The two simulated ΔPDFs are shown in Fig. 2b-c (details in Methods). The simulation with quantum excitation (Fig. 2b) is able to reproduce the shape of the experimental ΔPDF, including the early 1st shell OO contraction and the subsequent 2nd shell broadening. The simulation with classical excitation (Fig. 2c), on the other hand, predicts smaller changes in the structure and a delayed disordering of the 2nd shell compared to experiment and the quantum excitation. This comparison proves that accounting for the quantum distribution of the shared proton upon vibrational excitation is critical for correctly modeling the sub-picosecond dynamics of liquid water vibrational energy relaxation and redistribution. From here on, we focus on the quantum excitation simulation. In spite of the good match in shape between Fig.2a and b, the ΔPDF amplitude in the simulation is roughly a factor of two lower than that in the experiment. This mismatch could originate from uncertainty in the experimental excitation fraction, or from limitations in the MD simulations, such as the neglect of potential coherent vibrational excitation involving multiple O-H bonds or quantum effects in the relaxation dynamics. In fact, our approach assumes that the decoherence time of the collective vibrational excitation to be

faster than the excitation pulse.

The seemingly counterintuitive contraction-expansion behavior of the hydrogen bond is the result of both individual HB properties and the collective behavior of the HB network in water. In hydrogen bonded O-H…O systems, the O…O distance (R_1 here) decreases sharply as the O-H distance (r_1 here) increases. This behavior is observed experimentally[24] and explained by a number of theoretical models with various levels of complexity, such as the Lippincott–Schroeder model[5,25,26], simple proton donor-acceptor models[27], and an increase in the covalency of HB using bond order arguments[24,28]. Ultimately, it is a result of the coupling between the OH stretching and the HB motions. By exciting the system from the v_{OH}=0 to the v_{OH}=1 state, the expected value for the O-H distance is increased by 0.024 Å for the quantum Wigner distribution, twice as much as its classical counterpart (Extended Data Fig. 3). Based on these models, the r_1 expansion in the excited OH stretching quantum state will lead to a strong R_1 contraction. Therefore, the early HB contraction is a fundamental quantum-mechanical property of hydrogen-bonded systems during the excitation of the OH stretch that appears locally around the excited molecules. This motion also can be understood as the "intermolecular character" of the water vibration because of its appearance on the vibrationally excited v_{OH}=1 state. In addition, this contraction-expansion is responsible for the underdamped oscillatory behavior shown in the orange curve in Fig. 1f. On a longer timescale, energy is efficiently funneled from the stretching modes into all the degrees of freedom in water, leading to an increased temperature, HB weakening, and global R_1 expansion.

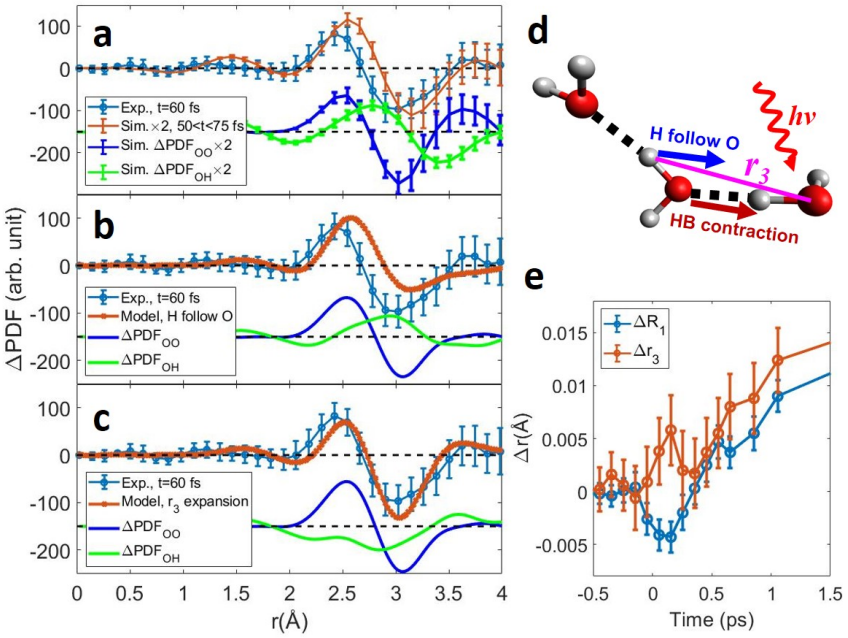

Fig. 3 | First shell hydrogen atom dynamics. a, The ΔPDF for experiment (t=60 fs) and simulation with quantum excitation (50<t<75 fs) with the simulation results amplified by a factor of two. **b-c,** The ΔPDF for two different models for the 1st shell hydrogen motion: **b,** hydrogen atoms follow parent oxygen atom (ΔR_1=Δr_2=Δr_3=-0.0036 Å); **c,** r_3 expansion (ΔR_1=Δr_2=-0.0041 Å, Δr_3=0.0038 Å). These values are obtained from the 1-parameter and 2-parameter χ^2 fittings (Fig. 2e and Fig. 3e). **d,** The ball-and-stick diagram for the H follow O model, corresponding to parts **a-b**. **e**, The fitted ΔR_1 and Δr_3 from experimental data. In parts **a-c**, the OO and OH components are plotted separately with a vertical shift, and the dashed lines represent the baselines. Exp., experiment, Sim., simulation. Error bars representing SEM of 60 independent measurements (Exp. in **a-c**), SEM of 200 independent simulations (Sim. in **a**), or the standard error from the fit (**e**).

Electron scattering is capable of resolving hydrogen atoms in water molecules[29]. Fig. 3a shows the experimental and simulated ΔPDF at around 60 fs, in which the simulation is able to reproduce all the major features of the experimental curve except the zero-crossing around 2.7 Å. In the previous analysis (Fig. 2e-f), we have used a minimalistic model that does not account for the motion of the 1st shell hydrogen atoms. Here we consider the hydrogen atom dynamics by additionally shifting r_3, the distance between the two 1st shell hydrogen atoms and the photoexcited oxygen atom (marked in Fig. 3d). In Fig. 3b we assume that the 1st shell hydrogen atoms follow the parent oxygen atom (Δr_3=ΔR_1), as shown by the ball-and-stick model in Fig.

3d. The ΔPDF predicted with this model somewhat matches with the simulation but disagrees with the experiment considerably, indicating that the 1st shell hydrogen atoms are not passively following their parent oxygen atom. Fig. 3c shows that the experimental ΔPDF can be better reproduced by an r_3 expansion model. To capture the r_3 as a function of time, we performed a two-parameter fitting, where ΔR_1 and Δr_3 are the two fitting parameters, Δr_2 is set to be equal to ΔR_1, and all other atom pair distances are unchanged (Methods). While this two-parameter model (Fig. 3e) more accurately reproduces the experimental findings during the first ~200 fs, to do so requires an unphysical expansion of the OH bond length in the central HB accepting molecules in Fig. 3d. This indicates the origin of the discrepancy between experiment and MD simulation results for more subtle intermolecular interactions. Potential origins of the discrepancy between theory and simulation include the lack of quantum effects in the Newtonian relaxation dynamics in simulation, the assumption of localized vibrational excitation in the present simulation, or the breakdown of the rudimentary pair distance-shifting model used for analyze the experimental data.

At later delay times, thermalization becomes the dominant source of the ΔPDF signal. In scattering experiments, the temperature of water can be characterized by g_2, the peak height of the 2nd OO shell in the radial distribution function[10]. Figure 4a shows the experimental g_2 and the corresponding temperature, using the calibration provided by Sellberg el al.[10] (Methods). The temperature starts to rise at ~300 fs and increases by 37.5±3.5 K over the 2.2-ps observation window. The time constant for the temperature rise is roughly 1 ps. The experimental ΔPDF at 2.2 ps is plotted in Fig. 4b, matching well with a simulated ΔPDF from two equilibrated water boxes with a temperature difference of 37 K. We have also measured the scattering signal and temperature evolution up to 100 ps, presented in Extended Data Fig. 1c (Methods).

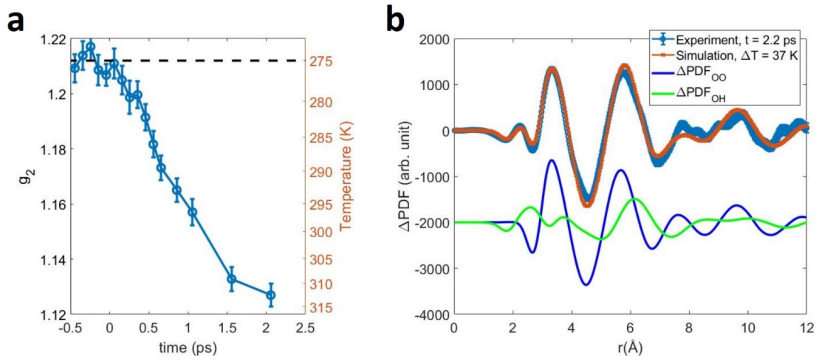

Fig. 4 | Thermalization. **a,** Experimental g_2, the peak height of the 2nd OO shell in the radial distribution function and corresponding temperature of water. **b,** The experimental ΔPDF at 2.2 ps and simulated ΔPDF from two equilibriated water boxes at 275 and 312 K. The ΔPDF_{OO} and ΔPDF_{OH} from simulation are plotted with a vertical shift for visibility. Error bars representing SEM of 60 independent measurements.

Our observations shed new light on the coupling between intra- and intermolecular vibrations in water. Early studies have been primarily focusing on the relaxation pathway of the water vibration, which showed that the strong Fermi resonance coupling between the stretching modes and the first overtone of the bending mode is a key step in OH stretch relaxation[3,7]. Recently, using ultrafast broadband 2D infrared spectroscopy, Ramasesha et al. have measured a unique spectral feature in the first ~50 fs[4], confirming the existence of intermolecular motions preceding vibrational relaxation, but the structural dynamics during this time remains unclear. In this experiment, we have identified the very first intermolecular structural response to be an OO contraction in the 1st coordination shell. Given OH stretching strengthens HB while both bending and libration weakens HB[30], the observed OO contraction suggests, counterintuitively, that the intermolecular structural reorganization (which involves the translational motion of the heavy oxygen atoms) occurs before the Fermi resonance coupling into the bending overtone (which only involves the motion of light hydrogen atoms). Our observation confirms that the strong coupling between intra- and intermolecular modes is a defining characteristic of water vibrational structure[4], and, in addition, provides a direct atomic resolution visualization of the intermolecular character of water vibration.

Data availability

Experimental data were generated at the MeV-UED facility at the SLAC National Accelerator Laboratory. Data behind each figure are available in Zenodo with the identifier DOI: 10.5281/zenodo.4678299. Raw datasets are available from the corresponding authors on reasonable request.

Code availability

The non-commercial codes used for the simulation and analysis here are available from the corresponding authors on reasonable request.

Acknowledgements We thank the helpful discussion with Thomas E. Markland. We thank Gregory M. Stewart for the help of making Fig. 1a. The experiment was performed at SLAC MeV-UED facility, which is supported in part by the DOE BES SUF Division Accelerator & Detector R&D program, the LCLS Facility, and SLAC under contract Nos. DE-AC02-05-CH11231 and DE-AC02-76SF00515. J. P. F. N., and M. C. are supported by the U.S. Department of Energy Office of Science, Basic Energy Sciences under Award No. DE-SC0014170. K. L. is supported by a Melvin and Joan Lane Stanford Graduate Fellowship and a Stanford Physics Department fellowship. J. Y. T. F. H., A. C., T. J. A. W., E. B., N. H. L., T. J. M., and K. J. G. were supported by the U.S. Department of Energy, Office of Science, Basic Energy Sciences, Chemical Sciences, Geosciences, and Biosciences Division. A.M.L. acknowledges support from the DOE BES Materials Science and Engineering Division under contract DE-AC02-76SF00515. Z. C. and M. M. are supported by the DOE Fusion Energy Sciences under FWP No. 100182.

Author Contributions

J. Y., K. J. G., A. M. L. and X. W. proposed the study. J. P. F. N., K. L., E. B., M. C., D. P. D.,

M. L., M. M., X. S., T. J. A. W. J. Y., A. A. C., and X. W. developed the experimental setup. M. E. K. developed the pump laser setup. J. Y., J. P. F. N., E. B., Z. C., A. A. C., T. F. H., K. L., M. L., M. M., X. S., T. J. A. W and X. W. performed the experiment. J. Y. analyzed the experimental data and performed the χ^2 fitting. J. Y., A. N., T. J. M., and K. J. G. interpreted the experimental data. R. D. and D. D. performed the pump-probe MD simulation. J. P. F. N. performed the equilibrium water simulation. N. H. L. and T. J. M. performed the 1D and 2D quantum simulations and the *ab-initio* electron scattering simulation. J. Y., R. D., N. H. L., D. D., T. J. M., K. J. G. and X. W. wrote the manuscript with inputs from all authors.

Competing interests The authors declare no competing interests.

Correspondence and requests for materials should be addressed to J. Y., D. D., K. J. G., T. J. M. and X. W.

Methods

LUES data collection

The experimental data was collected at the SLAC MeV-UED facility. The experimental setup was described in detail in a previous publication[16]. The neat water was delivered through a gas-accelerated liquid jet[17], under a flow rate of 0.20 mL/min and a helium carrier gas pressure of 72 psi. The sample thickness at the interaction point was measured to be ~100 nm using an optical interferometer. The electron beam was accelerated to a kinetic energy of 3.7 MeV using an rf-type photoinjector[31]. Each electron pulse contained roughly 60,000 electrons per pulse at the photocathode, and roughly 3,000 electrons per pulse at the sample location. The electron beam size was 88 (horizontal) × 37 (vertical) μm FWHM, measured by a knife-edge scan. The transmission of the electron beam after the liquid sheet was measured to be ~90%. The scattering patterns were recorded on a phosphor screen-based detector. In this experiment, the accessible Q range is 0.2 to 11.8 $Å^{-1}$. A 2.9 mm diameter hole was drilled in the center of the phosphor screen to transmit the unscattered electron beam. The small angle scattering signal was obtained by intentionally off-center the scattering pattern on the phosphor screen.

The 3.018 μm pump laser pulse was generated by pumping a commercial optical parametric amplifier with a 800 nm pulse generated from a Ti:Sapphire laser system. The energy on the sample was roughly 22 μJ, the spot size was 360 (horizontal) × 430 (vertical) μm FWHM, measured by a knife-edge scan. The spectrum of the pump laser was not directly measured due to the equipment limitation, but the spectra of the 2nd and the 3rd harmonic were measured after a BBO crystal. The 2nd harmonic was centered at 1.509 μm with a bandwidth of 25 nm FWHM, and the 3rd harmonic at 1.003 μm with a bandwidth of 17 nm FWHM, as shown in Extended Data Fig. 1b. The pulse duration was not measured but estimated to be between 100 and 150 fs FWHM. The pump fluence was estimated to be around 18 mJ/cm^2. The initial temperature, 275±10 K, was determined through a fitting of static scattering pattern to a classical force-field simulation, detailed in a previous publication[16]. The electron pulse and the pump laser pulse were operated at a repetition rate of 360 Hz. The IRF is between 209±4 fs (previous measurement[16]) and 224±32 fs (fastest signal in the current dataset).

We have also measured experimental data up to a delay time of 100 ps using a step size of 10 ps in a separate dataset under similar experimental conditions. For this dataset, the electron gun is operated under a "high charge mode", where the charge per electron pulse is a factor of 2-3 higher but the overall temporal resolution is degraded to > 500 fs. From this dataset we extracted the temporal evolution of g_2 and temperature using the same method as in Fig. 4a in the main text, shown in Extended Data Fig. 1c. The measurement shows that temperature rapidly increases in the first 10 ps and slowly recovered in the rest of the observation window. The temperature increased ~25 K at 100 ps. The final temperature increase can be used to estimate the excitation ratio α_{ex} using $\alpha_{ex} = 9\Delta T_{final} / T_{photon}$, where ΔT_{final} is the final temperature increase of the sample, T_{photon}=4767 K is the photon energy, and 9 is the number of degrees of freedom in the system.

The excitation ratio was estimated using three methods

1. 4.7%, from Beer-Lambert law using the pump fluence and the peak molar absorption coefficient measured by Bertie and Lan[32].
2. 4.7%, using the 25K temperature increase measured in scattering signal at 100 ps delay.
3. 7.1%, using the 37K temperature increase measured in scattering signal at 2 ps delay.

Since the first two methods agree with each other, and 2 ps is likely to be too short for reaching a complete thermal equilibrium, we use 5% as an estimated excitation ratio in the main text. However, each of the three methods above is subject to experimental uncertainties, which might partially contribute to the factor-of-two disagreement in amplitude between experiment and simulation shown in Fig. 2a-b in the main text. The uncertainty in excitation ratio does not alter the main conclusion of this work. If the excitation fraction is 7% instead of 5%, the amplitude of the initial HB contraction will be ~0.03 Å rather than ~0.04 Å.

Scattering pattern processing

The scattering intensity $I(t; Q)$ is generated through a standard processing procedure of baseline subtraction, center finding, normalization and radial average.

The difference scattering curve $Q\Delta S(t; Q)$ is calculated using the following equation

$$Q\Delta S(t;Q) = Q\frac{I(t;Q) - I_{ref}(t<0;Q)}{\left[\sum_{\alpha=1}^{3} f_\alpha(Q)\right]^2} \quad (1)$$

where $I_{ref}(t<0; Q)$ is a reference pattern that is taken before time zero, the sum over α is performed over the three atoms in a water molecule and $f_\alpha(Q)$ is the modified atomic scattering factor[10,33]. Here the modified atomic scattering factors are computed using a similar method as Sorenson et al.[33], but adapted for electron scattering using the Mott-Bethe formula[34]:

$$f_\alpha(Q) = \frac{Z - [1 + (a_\alpha - 1)exp(-Q^2/2\delta^2)]f_\alpha^X(Q)}{Q^2} \quad (2)$$

where Z is atomic number (8 for oxygen, 1 for hydrogen), a_α is partial charge scaling factor (1.11 for oxygen, 0.56 for hydrogen), δ=2.2Å^{-1}, and f_α^X is the atomic form factor under the

independent atom model for X-ray scattering, taken from Hubbell et al.[35].

The time zero in the experimental data is determined by the peak location of a Gaussian fitting to the low-Q signal shown in Fig. 1e in the main text.

Fourier-sine transform to calculate ΔPDF

The ΔPDF can be calculated through a Fourier-sine transform of $Q\Delta S(t; Q)$, as explained by Ihee et al.[14,18]:

$$\Delta PDF(t; r) = r \int_{Q=1}^{Q_{max}} Q\Delta S(t; Q) sin(Qr) e^{-0.03Q^2} dQ \quad (3)$$

where $e^{-0.03Q^2}$ is a damping term to avoid edge effects in the transform and is equivalent to a Gaussian smoothing in the real space. Only Q > 1 Å^{-1} is used in equation (3) to avoid the contribution from the inelastic component at low Q. Q_{max} in this experiment is 11.8 Å^{-1}. The experimental damped $Q\Delta S$ is plotted in Extended Data Fig. 1d, which shows the high-Q noises in Fig. 1c are mitigated. The PDF(r) and ΔPDF(t; r) used in the main text represent the probability of finding an atom pair at any distance r. The radial distribution function (RDF) $g(r)$, widely used in the literature and used in this work to make Fig. 4a in the main text, represents the probability of finding an atom pair in a unit volume at any distance r. The relation between the two representations, up to a scaling factor, is given by:

$$PDF(r) = 4\pi r^2[g(r) - 1] \quad (4)$$

One-parameter and two-parameter χ^2 fitting

In the main text, we used a one-parameter (Fig. 2e) and a two-parameter (Fig. 3c) standard χ^2 fitting to extract bond distance changes. In the one-parameter fitting, a simple shift ΔR_1 is introduced to the $g(r)$ for both the 1st OO shell (R_1) and the hydrogen bonded OH pairs (r_2), and the $g(r)$ for all other atom pairs are unchanged. From this modified $g(r)$, a scattering pattern is simulated (see **Equilibrium water simulation** section below), and then a ΔPDF is calculated from the simulated scattering pattern using equation (3) above. Several examples of the shifted $g(r)$ and ΔPDF are shown in Extended Data Fig. 4. The simulated ΔPDF is compared to the experimental ΔPDF and the result corresponding to minimum χ^2 value is returned as the fitting output. To exclude contributions from the covalent bond OH, the 2nd OO shell and other atom pairs, only distances between 1.5 and 3 Å are used for the fit. The two-parameter fitting includes an additional parameter Δr_3 that additionally shifts $g_{OH}(r)$ for r>2.5 Å, representing the change of the 1st shell OH distance, with all other conditions identical to the one-parameter fitting. The χ^2 is calculated through:

$$\chi^2 = \int_{r_{min}}^{r_{max}} \frac{(c_s\Delta PDF_{sim}(r,t) - \Delta PDF_{exp}(r,t))^2}{\sigma(r,t)^2} dr \quad (5)$$

where r_{min}=1.5 Å, r_{min}=3 Å, ΔPDF_{sim} and ΔPDF_{exp} are the simulated and experimental ΔPDF. c_s is a global scaling factor between experimental and simulation that is obtained by matching the 1st OO shell peak in charge-pair-distribution-function (next section in Methods, Extended

Data Fig. 5a). σ is the standard deviation of experimental data.

g_2 and temperature extraction

In Fig. 4 in the main text, we used g_2, i.e., the peak height of the 2nd OO shell in the RDF, to extract the temperature for each delay time. To extract g_2, we need to directly analyze the raw scattering patterns rather than the difference scattering patterns. This requires proper treatment of both the inelastic and structureless atomic scattering background.

In a recent paper, we have proposed a charge-pair-distribution-function (CPDF) that can be obtained directly from the raw patterns with neither atomic form factors nor background removal[36].

$$CPDF(t;r) = r\int_{Q=0}^{Q_{max}} Q^5 I(t;Q) sin\,(Qr) e^{-kQ^2} dQ \quad (6)$$

The advantage of this method is that the contribution from inelastic and other forms of background are concentrated at r<~2 Å, and thus does not affect the peak height of the 2nd shell at ~4.4 Å. The disadvantage is that each peak has two negative shoulders on each side. This disadvantage is not an issue for extracting the height of a single peak. A comparison of the static water data and simulation is given in Extended Data Fig. 5a, showing that experimental CPDF captures the 1st to the 4th OO shells. Extended Data Fig. 5b shows that the inelastic contribution in CPDF is limited to r<2.5 Å. The CPDF analysis also provides a method to scale the simulated and experimental data based on the raw PDF, so that the analyses on ΔPDF is scaled independently. In this work, this scaling factor c_s was obtained by matching the height of the first OO peak in Extended Data Fig. 5a between experiment and theory. The obtained c_s was applied to both the χ^2 fitting and the temperature analyses.

The extracted CPDF at five different time windows are shown in Extended Data Fig. 5c. Once the height of the 2nd OO shell in CPDF is determined (Extended Data Fig. 5d), the g_2 can be determined with two calibration points. Here we use: 1) the starting temperature (t<0) was 275 K (see "LUES data collection" section in Methods); and 2) CPDF=0 corresponds to g_2=1 by definition.

Equilibrium water simulation

The static water is modeled by classical MD with 4054 molecules in a 50 × 50 × 50 Å boxes in GROMACS software suite using the TIP4P-Ew force-field[37], which has been demonstrated for the prediction of static water structure for both electron scattering[16] and X-ray scattering[37] experiments. TIP4P-Ew force-field for equilibrium water simulations is chosen to maintain consistency with our previous work[16] on static water analysis and determine the initial temperature of the sample. We have verified that, the neural networks potential(NNP)[21], used for pump-probe simulation to achieve a higher accuracy for the femtosecond dynamics, provides results in good agreement with experiments and consistent with TIP4P-Ew in the short range (r<6 Å). However, the NNP does not provide accurate ΔPDF for r>6 Å (Extended Data Figure 6). This may be due to the short-range nature of the NNP, which is cut off at 6.36 Å and

Deleted: because the NNP was trained against a set of simulated trajectories that was computed using only 64

does not incorporate long-range electrostatics and van der Waals terms[21]. In the main text, simulations in Fig. 1b and Fig. 4b are carried out with TIP4P-Ew force-field, and simulations in Fig. 2b-c and Fig. 3a are carried out with the neural network potential.

Deleted: molecules

The classical MD trajectories were transformed into time-averaged RDF $g(r)$ using the VMD package[38,39], and the elastic scattering pattern was simulated using a formula given by Dohn et al[40],

$$I_{elastic}^{Electron}(Q) = \sum_l N_l f_l(Q)^2 + \sum_{l,m} f_l(Q) f_m(Q) \frac{N_l(N_m - \delta_{l,m})}{V} \times \int_0^{R_{box}} 4\pi r^2 \left[g_{l,m}(r) - 1 \right] \frac{\sin(Qr)}{Qr} \frac{\sin\left(\frac{\pi r}{L}\right)}{\frac{\pi r}{L}} dr \quad (7)$$

where the indices l, m are the type of atoms (O and H here), N_l is the number of atom type l, $f_l(Q)$ is the atomic form factor for l, $\delta_{l,m}$ is the Kronecker delta function, V is the volume of the simulation box, R_{box} is the length of the simulation box, $g_{l,m}(r)$ is the RDF of atom pair lm and L is half the length of the simulation box. The first term is the atomic component that does not contain structural information, and the second term is the molecular component that contains structural information.

The inelastic scattering cross-sections for electron and X-ray are related as[41]:

$$I_{inelastic}^{Electron}(Q) = Q^{-4} I_{inelastic}^{X-ray}(Q) \quad (8)$$

where X-ray scattering is expressed in units of the Thompson X-ray scattering constant, and electron scattering is expressed in units of the characteristic Rutherford constant. The Q^{-4} factor comes from the r^{-1} Coulomb potential[34]. The simulated inelastic scattering form factor (Fig. 1b in the main text) is obtained by adopting the singles- and doubles- configuration interaction quantum chemical simulation from Wang et al.[42] with the Q^{-4} factor applied. Once the scattering pattern is simulated, we use the same method as the experimental data analysis (equation (1) and equation (3)) to calculate the PDF and ΔPDF.

To validate the routine of RDF→scattering pattern→PDF, we compared the ΔPDF calculated both through this routine, and directly using equation (4) then a smoothing by convoluting with a Gaussian kernel. The result is shown in Extended Data Fig. 7a-c.

Pump-probe MD simulation

To model the pump-probe experiment, MD simulations were carried out with periodic boundary conditions on a cubic box with side length of 25.05 Å, containing 522 water molecules, corresponding to a density of ρ=0.994 g/cm3. Water molecules were modeled according to the neural networks potential[21] (NNP) trained on *ab initio* MD (AIMD) water structures based on the revised Perdew–Burke–Ernzerhof (RPBE)[43] density functional with vdW corrections using the D3 method[44]. This machine-learning potential accurately represents the *ab initio* potential-energy surface of water and overcomes the bottleneck of the high computational costs and cubic scaling of AIMD simulations. Moreover, by adopting the vdW corrections, which consist of atom-pairwise specific dispersion coefficients and cutoff radii computed from first principles, NNP-based simulations are able to correctly predict the density

maximum and melting temperature of water[21].

The system was initially prepared at 300 K with an NVT run by means of stochastic velocity rescaling[45] for 200 ps. After this run, additional 200 ps at 300K were performed, saving the atomic configuration (positions + velocities) every ps, in order to obtain the 200 independent replicas. Two different approaches, referred to as 'classical' and 'quantum', were used to model the excitation induced by the IR pump. In each case, 5% of the molecules (i.e. 26 molecules) were randomly excited following the experimentally estimated excitation ratio.

In the classical sampling, the molecules were excited by means of the generalized Langevin equation (GLE) thermostat[22,23].The GLE implements a non-Markovian dynamics by introducing history-dependent terms[46] in the standard Langevin equation. In this implementation, it is designed with a standard white noise Langevin thermostat with friction γ_{base} and target temperature T_{base}, and a δ-thermostat[47] at a temperature T_0 that is coupled with a friction parameter γ_0[22,23]. The memory kernel power spectrum reads as

$$K(\omega) = 2\gamma_{base} + \frac{\gamma_0}{\pi}\frac{\omega_0 \Delta\omega\omega^2}{\left(\omega^2-\omega_0^2\right)^2+\Delta\omega^2\omega^2} \quad (9)$$

The parameters were chosen to be γ_0^{-1} = 0.5 ps, γ_{base}^{-1} = 1 ps, and Δω = 1 cm^{-1}, and an online tool to generate the input matrices for the GLE thermostat can be found at http://gle4md.org/. The thermostat was tuned at the OH stretch frequency (e=3531 cm^{-1}, computed from the Fourier transform of the velocity-velocity autocorrelation function) of the H_2O vibrational spectrum. 5% of water molecules were excited with an excitation temperature T_0=4500 K, for 100 fs. This 'classical' excitation raises the instantaneous kinetic temperature of the OH stretch by ~3000 K, due probably to the anharmonic coupling between the OH bond stretch and the HOH angle bending, which does not guarantee a perfect adiabatic thermalization of the stretching mode. However, such coupling does not interfere with the relaxation dynamics[22,23] The first delay point after the 100-fs excitation phase is used as a reference point to calculate the difference signals in the main text figures.

Within the approximation of distinguishable particles, the path integral formalism enables a variety of approaches to sample equilibrium nuclear quantum distributions and dynamics[48-50]. Conversely, modeling vibrational excitation and relaxation at a quantum mechanical level still poses a severe methodological challenge. Here we opt for a semi-classical approach in which the quantum excitation is modeled according to the Wigner distribution function and the relaxation is classical. This approach is justified by the verification that zero-point energy leakage is slower than the sub-picosecond time scale of the local hydrogen-bond relaxation dynamics observed in the experiments (see section "**Zero-point energy leakage time**" below).

In the quantum sampling, the excitation process was assumed instantaneous and localized to one of the two OH bonds with initial conditions for the excited OH stretch generated from the v_{OH}=1 Wigner distribution of the refined Lippincott–Schroeder model[5]. As shown by

comparing to 1D and 2D NNP based OH stretching potentials in a frozen-environment picture (See section "**2D stretching NNP vs. Lippincott-Schroeder model**" below), this model provides a simple yet reasonable 1D description of the OH stretch motion. This inter- and intramolecular localized initial condition sampling rests on the assumption that the vibrational decoherence time of the expectedly collective excitation is fast compared to the excitation pulse. Specifically, starting from the classically sampled equilibrium phase-space distributions, the displacement of the H atom along the excited OH bond in the excited molecules as well as the corresponding components of the atomic velocities of the O and H atoms were resampled from the v_{OH}=1 Wigner distribution of the Lippincott–Schroeder model by rejection sampling. The unexcited OH bonds in the excited molecules were resampled from the corresponding v_{OH}=0 Wigner distribution. The quantum sampling was restricted to the region of phase space with positive-valued Wigner distribution. To separate the effect of the excitation process from the change inevitably induced by replacing the classical with the quantum sampling, the ΔPDF calculations were computed with reference to simulations with initial conditions for both OH bonds in the excited molecules sampled from the v_{OH}=0 quantum distribution. The vibrational eigenstates were obtained from direct diagonalization of the Fourier Grid Hamiltonian on a position grid of 1024 points ranging from 0.8 to 4.0 a.u. The v_{OH}=0,1 eigenstates of the Lippincott–Schroeder model and the corresponding Wigner functions obtained by discrete inverse Fourier transform are shown in Extended Data Figure 2. The average between 0 and 25 fs of the v_{OH}=0 dynamics is used as a reference point to calculate the difference signals in the main text figures.

As shown in Extended Data Figure 8c, the quantum excitation brings the instantaneous kinetic temperature of the OH stretch to ~5500 K which is compatible with the photon energy of ~4800 K in the experiments. Nonequilibrium simulations were averaged over 200 independent replicas, where every replica is characterized by a different set of initial atomic positions, atomic velocities (as explained above) and by a different subset of excited molecules. The equations of motion are integrated with a time-step of δt=0.25 fs. Long-range electrostatic interactions are calculated using the particle-particle particle-mesh solver algorithm[51]. All simulations were carried with the LAMMPS simulation package[52].

In the simulations, the R_1 position (Fig. 2e-f) is calculated by means of a weighted average of the RDF $g_{OO}(r;t)$

$$R_1(t) = \frac{\int_{r_1}^{r_2} r g_{OO}(r;t) dr}{\int_{r_1}^{r_2} g_{OO}(r;t) dr} \tag{10}$$

where r_1 is 2.4 Å and r_2 is 3.3 Å, taken from the isosbestic points reported by Skinner et al.[19].

Determining instantaneous kinetic temperature from pump-probe MD simulation

Instantaneous kinetic temperature of vibrational modes was computed by considering specific

components of the atomic velocities. The temperature of OH stretching modes was computed by projecting the difference between oxygen and hydrogen velocities on the unit vector identifying the OH bond,

$$T_{stretch} = \frac{2}{k_B} \cdot \frac{\mu}{2} \left[(v_O - v_H) \cdot \frac{\vec{d_{OH}}}{d_{OH}} \right]^2 \quad (11)$$

where μ is the reduced mass for O and H atoms, $\vec{d_{OH}}$ is the vector pointing from O atom to H atom, v_O and v_H are the velocities for O and H atoms. The temperature of rotational modes was calculated by considering only the hydrogen velocity components perpendicular to the OH bond, once the velocity of the molecular center of mass was subtracted

$$T_{rot} = \frac{1}{k_B} \frac{m_H}{2} \left[(v_H - v_{COM}) \times \frac{\vec{d_{OH}}}{d_{OH}} \right]^2 \quad (12)$$

where m_H is the mass of H atom, and v_{COM} is the velocity of the molecular center of mass. In this case, T_{rot} involves mostly bending and libration modes. The simulated temperature evolution for the quantum and classical excitation are shown in Extended Data Fig. 8.

Ab initio electron scattering simulation

The *ab initio* electron scattering is used to predict the inelastic and elastic signal change of the first vibrationally excited OH stretching state (v_{OH}=1) in comparison to the ground state (v_{OH}=0). The simulation (Extended Data Fig. 1a) is performed on a single isolated water molecule using an OH distance of 1.021 Å for the v_{OH}=1 excited bond and 0.994 Å for the unexcited (corresponding to v_{OH}=0,1 level at an R_1 distance of 2.80 Å) and 0.989 Å for v_{OH}=0 (R_1 distance of 2.85 Å), computed as position expectation values of the refined Lippincott–Schroeder model (see **Pump-Probe MD simulation** section above). Rotationally averaged elastic and inelastic scattering signals were computed at the complete active space self-consistent field level of theory with the aug-cc-pVDZ[53] basis set and an active space containing 8 electrons in 7 orbitals ($2a_1$, $3a_1$, $1b_2$, $1b_1$, $4a_1$, $2b_2$, $2b_1$). The signals were evaluated using a Q-grid ranging from 0.0 to 10.0 Å^{-1} (increments of 0.1 Å^{-1}) and a 590-point Lebedev quadrature using the implementation in the TeraChem program[54-56] presented in previous work[57]. Cosine and sine squared angular distributions were used to simulate the contribution from the excited and unexcited fractions, respectively. The simulation predicts a sharp increase of inelastic scattering that is maximized at Q=0 and significantly stronger than the change in elastic scattering at small Q. This sharply increasing $Q\Delta S$ signal as Q approaches 0 matches with both our $Q\Delta S$ data around time zero and the characteristic shape of inelastic electron scattering (see, e.g. Ref.[58]). For the $Q\Delta S$ signal at Q>1 Å^{-1}, they do not match the characteristic shape of inelastic scattering. Therefore, we concluded that they belong to the elastic component (see Fig. 1c caption) and were used in the Fourier-sine transform to compute ΔPDF.

2D stretching NNP vs. Lippincott-Schroeder model

In this section, we show that the Lippincott-Schroeder (LS) model provides a reasonable 1D representation of the OH-stretch motion in the NNP-based liquid water simulations, in spite of significant deviations at large OH distances. To this end, we consider only the OH stretching

Deleted: simple and

potential for a single water molecule with fixed bond angle and in a frozen environment. The 2D vibrational Hamiltonian (in a.u.) takes the form[59,60]

$$\hat{h}_{\mathrm{v}}^{2\mathrm{D}} = -\frac{1}{2\mu}\frac{\partial^2}{\partial R_1^2} - \frac{1}{2\mu}\frac{\partial^2}{\partial R_2^2} - \frac{\cos\theta}{m_{\mathrm{O}}}\frac{\partial^2}{\partial R_1 \partial R_2} + V(R_1, R_2; \theta) \qquad (13)$$

where R_1, R_2 and θ are the OH bond distances and HOH angle (see inset in Extended Data Fig. 9d), $\mu = \frac{m_{\mathrm{H}} m_{\mathrm{O}}}{m_{\mathrm{H}} + m_{\mathrm{O}}}$ is the reduced mass, where $m_{\mathrm{H}}(m_{\mathrm{O}})$ is the hydrogen (oxygen) mass, and $V(R_1, R_2; \theta)$ the ground-state 2D potential energy surface (PES) along the OH stretching modes at a fixed bond angle. The latter was computed using the NNP by displacing the OH bonds of a single water molecule while keeping the remaining degrees of freedom fixed. This was repeated for 200 configurations sampled from the initial NNP ground-state 300K NVT simulation (522 water, periodic boundary conditions, yielding an average OO distance of 2.92±0.01Å). Below, this frozen-phonon picture is referred to as the liquid-phase results. We further considered the corresponding "gas-phase" data generated by removing all but the central water molecule from each of the sampled configurations, i.e., using the liquid-phase distribution of HOH bond angles (104.1±4.4°). The diagonal/off-diagonal terms of the kinetic energy operator were represented with $4^{\mathrm{th}}/2^{\mathrm{nd}}$ order central finite differences. The stretching vibrational states of the electronic ground state were obtained by diagonalizing the 2D Hamiltonian discretized on a 95×95 real space grid ranging from 0.94 to 3.4 bohr in both directions.

Extended Data Fig. 9 shows the lowest eigenstates for a representative configuration in the gas-phase (top panel) and liquid-phase (bottom panel) as well as the distribution of frequencies (relative to the ground vibrational state) for the lowest excited vibrational states across all configurations. The heterogeneous H-bonding environment leads to a localization of the symmetric/antisymmetric stretching modes, a general red shift and broadening of the frequency distributions in liquid water. As indicated by the gray dashed line in Extended Data Fig. 9h, the $\Delta\nu_1$ frequency derived from the LS model overlaps well with the NNP-based frequency distributions. The 1D cuts along each OH bond for the NNPs (2×200) in gas-phase and liquid-phase are compared to the LS potential in Extended Data Fig. 9i. The counteracting effects of a less repulsive potential at short OH distances and steeper at longer distances for the LS model relative to the NNP explains their satisfactory agreement for the lowest stretching states considered in this work. Stark differences exist between the LS potential and the effective NNP in liquid phase when the OH distance exceeds 1.3 A. This discrepancy does not affect the v= 1 quantum excitation, which is the focus of this work, as such long OH distances are not sampled by the Wigner distribution, as shown in Extended Data Fig. 3a.

Zero-point energy leakage time

The MD simulation approach used to interpret the experimental results consists of a quantum excitation followed by a relaxation in which the dynamics is Newtonian. Hence, the observed relaxation dynamics, in principles, convolutes with the equilibration of a quantum distribution

to a classical state. To assess this effect, in particular the issue of zero-point-energy (ZPE) leakage, we have simulated the relaxation of a quantum ground state to the classical state by nonequilibrium MD. We prepared the quantum ground state using the generalized Langevin equation (GLE) approach, in which the memory kernel is designed to produce quantum corrections to the classical distribution of the positions and momenta of the nuclei[61,62]. To prepare our water simulation box (the same used for the non-equilibrium simulations, 522 molecules at a density of ρ=0.994 g/cm^3, here averaged over 10 independent replicas) in a quantum state, we equilibrated it for 20 ps using the quantum GLE thermostat. Eventually, the system was let free to evolve in the microcanonical ensemble for further 20 ps. During this relaxation run, the trajectories were sampled each timestep to calculate the mode projected kinetic temperature.

The reliability of the quantum GLE thermostat is assessed by computing the radial distribution function (RDF) over the last 10 ps of the trajectory, shown in Extended Data Fig. 10a-c. The description of structural features improves significantly when using the quantum thermostat, especially in the OH bond which shows a very good agreement *ab initio* PIMD results[63].

While in classical simulations all the degrees of freedom have the same energy according to equipartition, in the quantum GLE run the kinetic energy of the various degrees of freedom of the system is redistributed according to their oscillation frequency. We monitored this effect by computing the kinetic energy (in K) of intra- and intermolecular modes: OH stretching, molecular rotations and hindered translations. During the classical NVT run, all the degrees of freedom thermalize at 300 K, as expected from the equipartition theorem. The quantum GLE thermostat couples differently to different modes, as shown in Extended Data Fig. 10d, due to nuclear quantum effects, introducing large temperature gradients between low and high frequency modes. Here stretching modes equilibrate at $T_{stretch} = 1642 \pm 17K$, while the librations equilibrate at $T_{rot} = 590 \pm 9K$ and the center of mass motion at $T_{com} = 321 \pm 4K$ (Ext. Data Fig. 10e)[64].

When the thermostat is switched off, the kinetic energy redistributes among the modes due to ZPE leakage from internal modes. Extended Data Fig. 10e shows that an equilibrium temperature is reached within 8 ps and that the stretching mode follows a bi-exponential trend (inset), with the fastest relaxation time τ_1=0.8 ps and slowest τ_2=2.9 ps. Both values are significantly longer than the rapid structural relaxation effects observed in our ultrafast crystallography experiment as well as in the simulations. Furthermore, as the O-O rdf is the least influenced by the quantum GLE thermostat (Ext. Data Fig. 10a), its time evolution during the NVE relaxation is mainly driven by temperature effects: the RDF curves progressively move away from the NVT at T=300K one (Ext. Data Fig. 10f). When plotting the shift over time of the R_1 distance (inset), it shows an overall expansion of the first hydration shell as expected from the sample thermalization, which follows the energy redistribution among the vibrational modes.

Influence of initial energy with classical initial conditions

In order to better understand the origin of the difference between quantum and classical procedures to represent the initial conditions after excitation, we have repeated the hot-spot GLE simulations injecting the full v=1 energy, i.e. $E = \frac{3}{2}h\nu$ (which includes zero-point energy). The goal of this computer experiment is two-fold: on the one hand it shows the effect of varying the amount of energy injected in the classical simulations, on the other hand it provides a more direct comparison with the quantum simulations, as in the latter zero-point energy is also included, so that the overall energy in quantum excited molecules corresponds to $E = \frac{3}{2}h\nu$. Extended Data Fig.7d-f shows that for sub-picosecond time scales the ΔPDF of the new classical simulations remain very different from the quantum ones, thus indicating that it is not enough to provide more energy in a classical way to attain the fast de-excitation dynamics of water. For longer timescales (1-2 ps), when thermal relaxation sets in, the ΔPDF of the classical $\frac{3}{2}h\nu$ simulation is almost exactly equivalent to the one following the quantum excitation.

Relative brightness of OH and OO pairs

For electron scattering at 3.7 MeV, the elastic atomic cross section of the hydrogen atom is σ_H/σ_O=4.0% of that of the oxygen atom, calculated using ELSEPA[65] under the independent atom approximation. The contrast of OH and OO atom pairs in electron scattering can be estimated by:

$$\frac{I_{OH}}{I_{OO}} = 2\sqrt{\frac{\sigma_H}{\sigma_O}} = 40\% \quad (14)$$

where the factor of 2 comes from the fact that there are two hydrogen atoms and one oxygen atom in a water molecule.

Comparison to time-resolved X-ray scattering

Time-resolved X-ray scattering (TRXS) is a well-established experimental technique that can also measure atomic motions on picosecond (using synchrotrons) and femtosecond (using XFELs) timescale. Therefore, it is useful to discuss the key differences between LUES and TRXS, especially in the context of this particular experiment. For this experiment, four key differences are worth noting:

1. The available maximum Q range in this work is 11.8 Å^{-1} while the state-of-the-art TRXS with femtosecond resolution is roughly 6.5 Å^{-1}, using an XFEL with 12.7 KeV photon energy (See, e.g. Ref. [66]). A comparable Q range would require a photon energy of ~25 KeV. Such a photon energy is not yet demonstrated in TRXS experiments using XFELs, but is expected to be achieved in the near future (e.g. SLAC LCLS-II facility or European XFEL facility).
2. For liquid samples, one of the advantages of TRXS over LUES is the option of using a

regular round jet (with a typical thickness of 50-100 μm) rather than a flat jet (with a thickness of ~100 nm), thanks to its higher penetration depth. A thicker jet is much easier to operate under vacuum. However, this would not work for this particular experiment, because the penetration depth of the pump laser is only ~800 nm. This is to say that TRXS would have to use a flat jet as well. The combination of hard X-ray pulses from XFEL with ultrathin liquid jet in vacuum is a non-trivial technique that is still under R&D phase.

3. The small-angle inelastic scattering is a unique feature to electron scattering.
4. Protons are visible in LUES while not visible in TRXS thanks to the Coulomb interaction. Therefore, analyses in Fig. 3 will not be possible with TRXS.

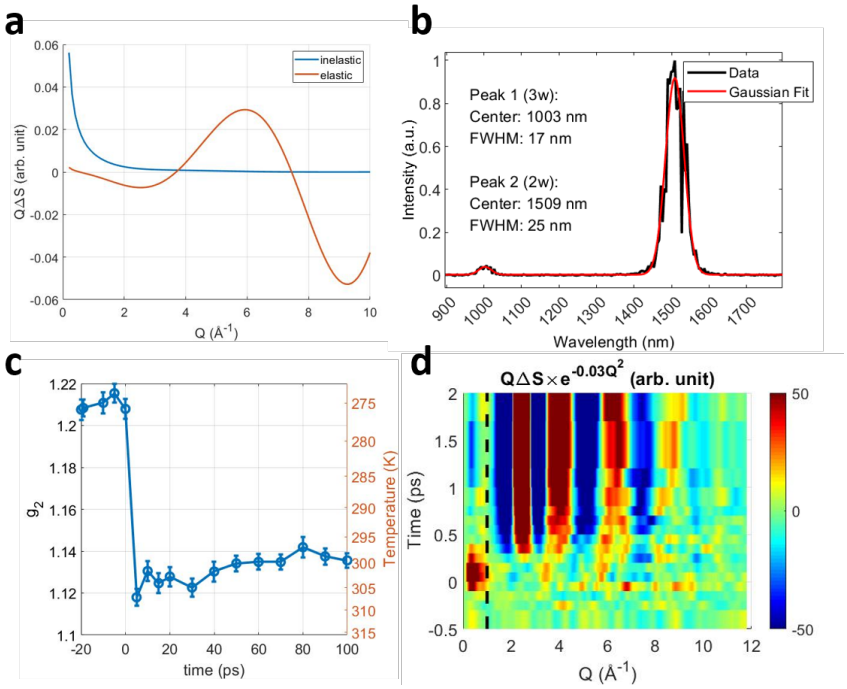

Extended Data Figure 1 | Extra information for data interpretation. (a) Ab initio simulation of the inelastic and elastic scattering signal change for v_{OH}=1 in comparison to v_{OH}=0. The simulation is performed on a single water molecule with OH bond lengths adjusted to the equilibrium length for each vibrational state as predicted by Bakker et al[5], more details see Methods. (b) Spectrum of the second and the third harmonics of the pump laser. (c) Experimental g_2 and temperature evolution up to 100 ps. (d) Damped $Q\Delta S$ from experimental data. This is related to the Fig. 1c in the main text by the damping term $e^{-0.03Q^2}$, see equation (3) in Methods.

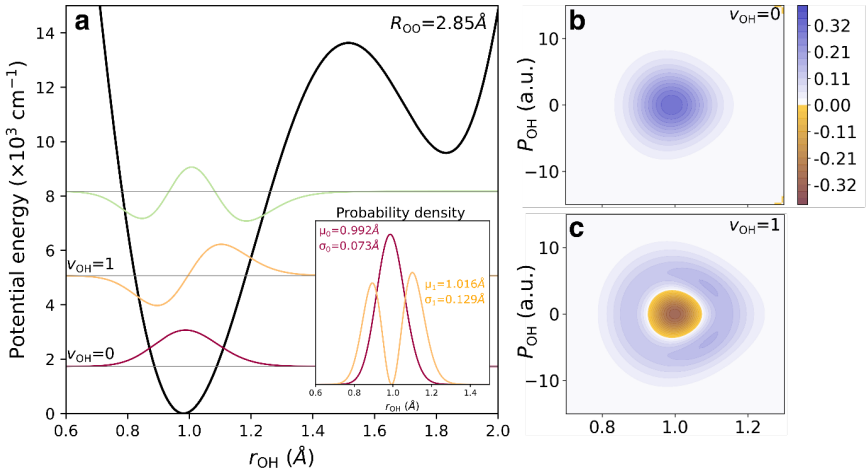

Extended Data Figure 2 | Wigner sampling. a, The three lowest eigenstates (colored lines) and eigenvalues (horizontal gray lines) of the Lippincott–Schroeder model potential (black line). Insert: the probability distribution of the v_{OH} =0 and v_{OH} =1 states, μ and σ represent mean and standard deviation. **b-c**, Wigner distribution for v_{OH} =0 and 1, respectively. The region of phase space with negative values of the v_{OH} =1 distribution (orange shades) was excluded from the sampling. Note the different color gradient used for negative function values. Lippincott–Schroeder model (R_{OO}=2.85 Å) is used for sampling of the initial displacements and velocities along the OH bonds of the excited molecules.

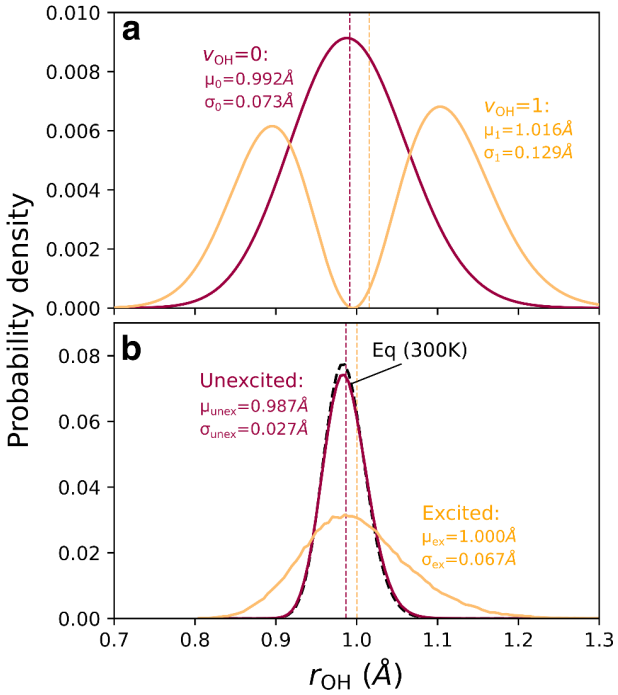

Extended Data Figure 3 | Probability density from classical and Wigner sampling. a, Wigner sampling. Magenta represents v_{OH}=0, yellow represents v_{OH}=1. **b,** Classical sampling. Magenta and yellow represent unexcited and excited molecules, respectively, calculated by averaging over the final 10-fs window during the excitation phase. Dashed black represents the equilibrium water before excitation. The vertical dotted lines represent the equilibrium distance for each curve, and μ and σ represent the mean and standard deviation of each curve, respectively.

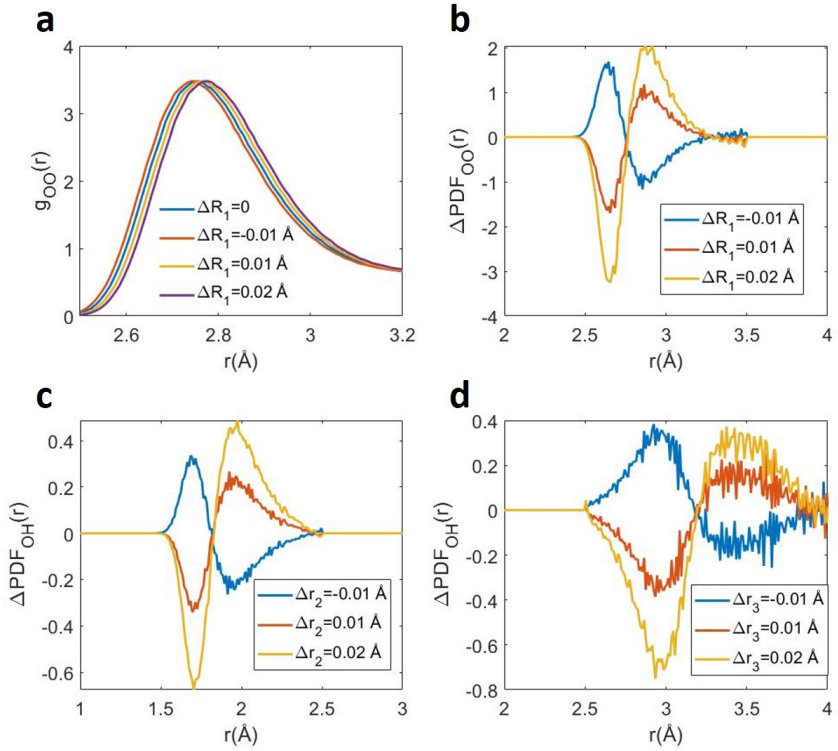

Extended Data Figure 4 | Examples of pair distances shift. a, $g_{OO}(r)$ around the 1st OO peak for four different ΔR_1. **b**, ΔPDF_{OO} for three different ΔR_1. **c**, ΔPDF_{OH} for three different Δr_2. **d**, ΔPDF_{OH} for three different Δr_3.

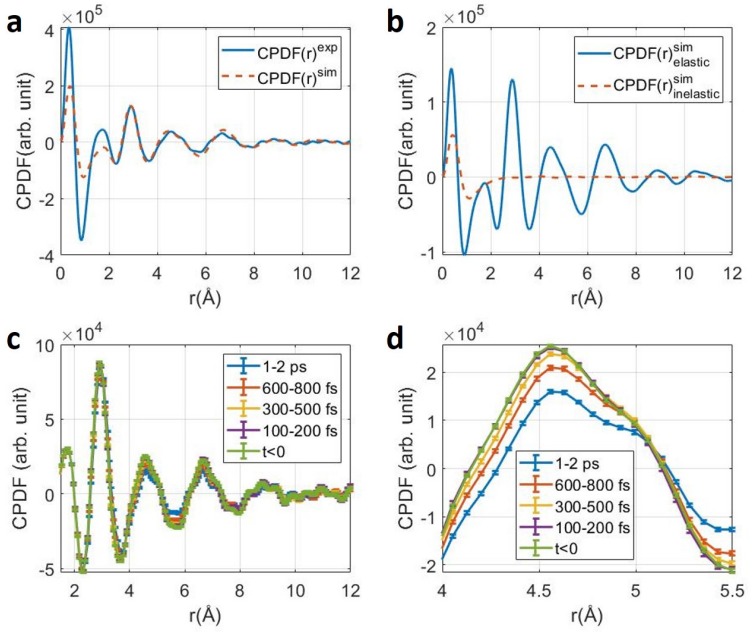

Extended Data Figure 5 | CPDF analysis (defined by equation (6), see Methods). a, A comparison of experimental and simulated CPDF. The overall scaling factor is achieved by matching the height of the 1st OO between experimental and simulated curves. The simulation is a 275 K water box under equilibrium condition. **b,** The simulated elastic and inelastic components of the CPDF, the inelastic component is concentrated to r<2.5 Å. Sim. = simulated. Exp. = experimental. **c,** CPDF for five delay windows (labeled in the legend) in full r range. **d,** CPDF for five delay windows (labeled in the legend) around the 2nd OO shell. The peak height around 4.6 Å is used to extract g_2 for Fig. 4a in the main text.

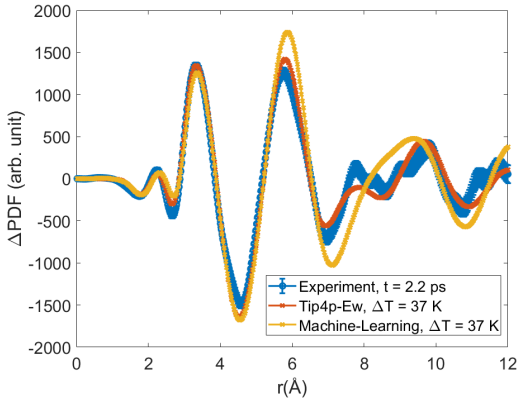

Extended Data Figure 6 | Comparison of equilibrium ΔPDF simulation. ΔPDF from experiment at 2.2 ps (blue with error bars), simulation using Tip4p-Ew force field (orange) and simulation using machine-learning force field (yellow).

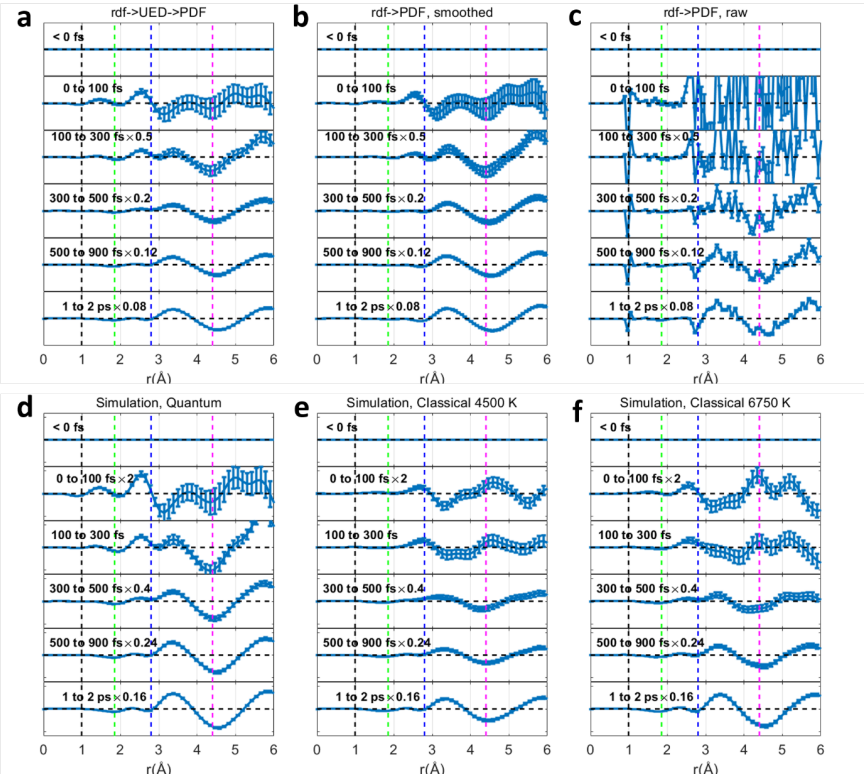

Extended Data Figure 7 | ΔPDF simulated using different methods. a-c, ΔPDF consistency. **a,** The ΔPDF simulated using the conventional method, i.e. by first simulating the electron scattering pattern using equation (7), then transforming to real space using equation (3). **b,** The ΔPDF simulated by directly applying equation (4), and smoothed by convolution with a Gaussian kernel with a FWHM of 0.53 Å. The weight of OO, OH and HH pairs are chosen to be 1, 0.4 and 0.16, respectively, obtained by atomic scattering cross section and the relative number of each types of atom pairs. The 0.53 Å FWHM of the Gaussian Kernel is obtained using $2\pi/Q_{max}$, where Q_{max}=11.8Å^{-1} is the maximum Q range in this experiment. **c,** The ΔPDF simulated by directly applying equation (4) without Gaussian smoothing. The vertical scales of all sub-panels are identical. **d-f**, Comparison of the ΔPDF in quantum simulations (d), classical simulations with $h\nu$ excitation (e) and classical simulations with 3/2 $h\nu$ excitation (f).

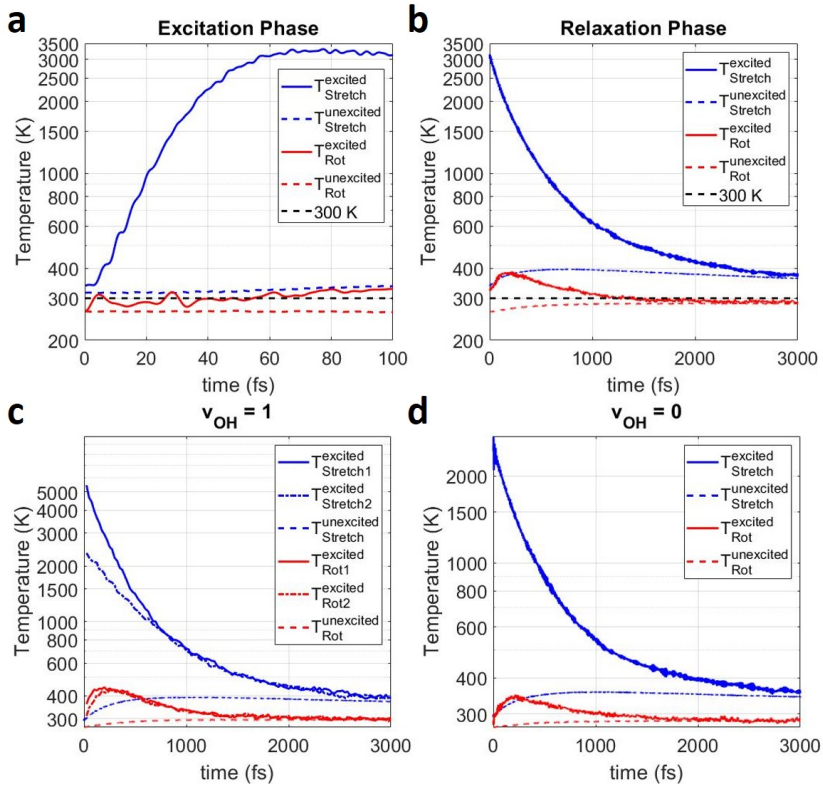

Extended Data Figure 8 | Simulated instantaneous kinetic temperature evolution. a-b, classical excitation. **a,** During the 100-fs excitation phase. **b,** during the 3-ps relaxation phase. **c-d,** quantum excitation. **c,** v_{OH} =1. **d**, v_{OH} =0. $T_{stretch}$ and T_{rot} are defined in equations (11) and (12). In part **c**, the subscript "Stretch1" and "Rot1" indicate the OH bond corresponding to v_{OH} =1 Wigner sampling, and the "Stretch2" and "Rot2" indicate the OH bond corresponding to v_{OH} =0 Wigner sampling. The superscript "excited" indicates Wigner sampling. Excited and unexcited molecules are calculated separately. The initial temperature before excitation is 300 K.

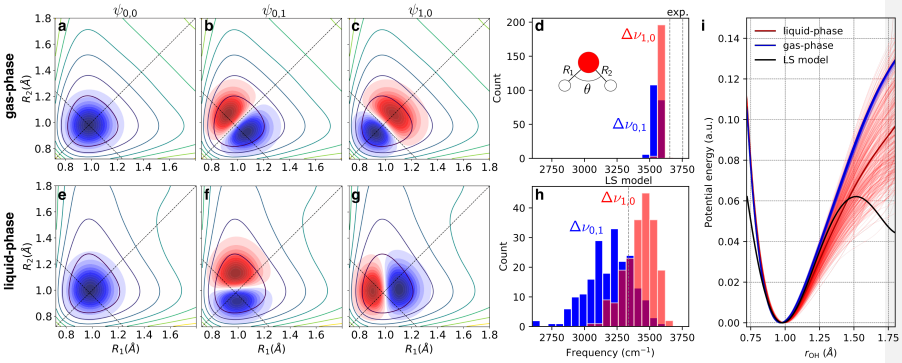

Extended Data Figure 9 | Comparison of NNP-based 2-D OH stretching vibrational modes in "gas-phase" (top panels) and "frozen-phonon" liquid phase (bottom panels). (a-c) and (e-g) correspond to the lowest vibrational eigenstates (n_1, n_2) for a representative configuration (bond angle of 104.4°) among the 200 2-D PESs considered. The dashed black lines indicate symmetric and antisymmetric displacements. (d, h) Distribution of vibrational frequencies (defined as $\Delta\nu_{n_1,n_2} = \nu_{n_1,n_2} - \nu_{0,0}$) for the two lowest OH stretching vibrationally excited states for the 200 configurations. The distribution in the gas-phase originates from the variation in the bond angle. The vertical lines indicate the experimental gas-phase stretch frequencies[67] and $\Delta\nu_1$ from the 1-D Lippincott-Schroeder model, respectively. (i) Comparison of 1-D OH stretch potentials for gas-phase and liquid water as obtained from the NNP (blue and red, respectively) and the Lippincott-Schroeder model (black). The transparent thin lines correspond to the underlying 2×200 NNP replicas while the corresponding thick lines indicate the average potentials.

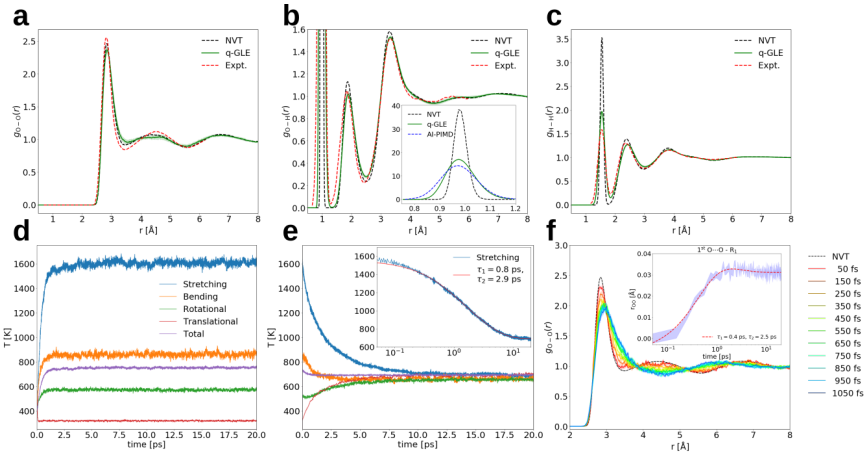

Extended Data Figure 10 | Zero-point energy leakage time. (a-c) A comparison for the (a) OO, (b) OH and (c) HH RDFs computed during an equilibrium run for a classical distribution of positions and momenta (NVT), during the coupling with the quantum GLE thermostat, from ab initio PIMD simulations[63] and measured from neutron diffraction experiments[68]. The inset in (b) is a zoom-in on the OH bond peak where, due to the absence of experimental data to compare with, we reported the comparison with DFT-based PIMD simulations. (d) Kinetic energies computed during the coupling with the quantum thermostat. (e) Kinetic energies computed during the NVE simulations. The inset in (d) shows a temporal fitting of the stretching temperature decay. (f) Time-resolved RDF computed during the NVE relaxation. The black curve refers to the NVT-computed RDF, obtained at T=300 K. The inset shows the shift of the R_1 distance during the system relaxation.

References

1 Stillinger, F. H. Water Revisited. *Science* **209**, 451-457, doi:10.1126/science.209.4455.451 (1980).

2 Perakis, F. *et al.* Vibrational Spectroscopy and Dynamics of Water. *Chem. Rev.* **116**, 7590-7607, doi:10.1021/acs.chemrev.5b00640 (2016).

3 Lindner, J. *et al.* Vibrational relaxation of pure liquid water. *Chem. Phys. Lett.* **421**, 329-333, doi:https://doi.org/10.1016/j.cplett.2006.01.081 (2006).

4 Ramasesha, K., De Marco, L., Mandal, A. & Tokmakoff, A. Water vibrations have strongly mixed intra- and intermolecular character. *Nat. Chem.* **5**, 935-940, doi:10.1038/nchem.1757 (2013).

5 Bakker, H. J. *et al.* Transient absorption of vibrationally excited water. *J. Chem. Phys.* **116**, 2592-2598, doi:10.1063/1.1432687 (2002).

6 Fecko, C. J., Eaves, J. D., Loparo, J. J., Tokmakoff, A. & Geissler, P. L. Ultrafast Hydrogen-Bond Dynamics in the Infrared Spectroscopy of Water. *Science* **301**, 1698-1702, doi:10.1126/science.1087251 (2003).

7 Ashihara, S., Huse, N., Espagne, A., Nibbering, E. T. J. & Elsaesser, T. Ultrafast Structural Dynamics of Water Induced by Dissipation of Vibrational Energy. *The Journal of Physical Chemistry A* **111**, 743-746, doi:10.1021/jp0676538 (2007).

8 Auer, B. M. & Skinner, J. L. IR and Raman spectra of liquid water: Theory and interpretation. *J. Chem. Phys.* **128**, 224511, doi:10.1063/1.2925258 (2008).

9 Amann-Winkel, K. *et al.* X-ray and Neutron Scattering of Water. *Chem. Rev.* **116**, 7570-7589, doi:10.1021/acs.chemrev.5b00663 (2016).

10 Sellberg, J. A. *et al.* Ultrafast X-ray probing of water structure below the homogeneous ice nucleation temperature. *Nature* **510**, 381-384, doi:10.1038/nature13266 (2014).

11 Beyerlein, K. R. *et al.* Ultrafast nonthermal heating of water initiated by an X-ray Free-Electron Laser. *Proceedings of the National Academy of Sciences of the United States of America* **115**, 5652-5657, doi:10.1073/pnas.1711220115 (2018).

12 Wen, H., Huse, N., Schoenlein, R. W. & Lindenberg, A. M. Ultrafast conversions between hydrogen bonded structures in liquid water observed by femtosecond x-ray spectroscopy. *J. Chem. Phys.* **131**, 234505, doi:10.1063/1.3273204 (2009).

13 Perakis, F. *et al.* Coherent X-rays reveal the influence of cage effects on ultrafast water dynamics. *Nature Communications* **9**, 1917, doi:10.1038/s41467-018-04330-5 (2018).

14 Kim, K. H. *et al.* Direct observation of bond formation in solution with femtosecond X-ray scattering. *Nature* **518**, 385-389, doi:10.1038/nature14163 (2015).

15 van Driel, T. B. *et al.* Atomistic characterization of the active-site solvation dynamics of a model photocatalyst. *Nat. Commun.* **7**, 13678, doi:10.1038/ncomms13678 (2016).

16 Nunes, J. P. F. *et al.* Liquid-phase mega-electron-volt ultrafast electron diffraction. *Struct. Dyn.* **7**, 024301, doi:10.1063/1.5144518 (2020).

17 Koralek, J. D. *et al.* Generation and characterization of ultrathin free-flowing liquid sheets. *Nature Communications* **9**, 1353, doi:ARTN 1353
10.1038/s41467-018-03696-w (2018).

18 Ihee, H. Visualizing Solution-Phase Reaction Dynamics with Time-Resolved X-ray Liquidography. *Acc. Chem. Res.* **42**, 356-366, doi:10.1021/ar800168v (2009).

19 Skinner, L. B., Benmore, C. J., Neuefeind, J. C. & Parise, J. B. The structure of water around the compressibility minimum. *J. Chem. Phys.* **141**, 214507, doi:10.1063/1.4902412 (2014).

20 Haldrup, K. *et al.* Observing Solvation Dynamics with Simultaneous Femtosecond X-ray Emission

Spectroscopy and X-ray Scattering. *The Journal of Physical Chemistry B* **120**, 1158-1168, doi:10.1021/acs.jpcb.5b12471 (2016).

21 Morawietz, T., Singraber, A., Dellago, C. & Behler, J. How van der Waals interactions determine the unique properties of water. *Proc. Natl. Acad. Sci. U.S.A.* **113**, 8368-8373, doi:10.1073/pnas.1602375113 (2016).

22 Dettori, R. *et al.* Simulating Energy Relaxation in Pump–Probe Vibrational Spectroscopy of Hydrogen-Bonded Liquids. *J. Chem. Theory Comput.* **13**, 1284-1292, doi:10.1021/acs.jctc.6b01108 (2017).

23 Dettori, R., Ceriotti, M., Hunger, J., Colombo, L. & Donadio, D. Energy Relaxation and Thermal Diffusion in Infrared Pump–Probe Spectroscopy of Hydrogen-Bonded Liquids. *J. Phys. Chem. Lett.* **10**, 3447-3452, doi:10.1021/acs.jpclett.9b01272 (2019).

24 Gilli, P., Bertolasi, V., Ferretti, V. & Gilli, G. Evidence for resonance-assisted hydrogen bonding. 4. Covalent nature of the strong homonuclear hydrogen bond. Study of the O-H--O system by crystal structure correlation methods. *Journal of the American Chemical Society* **116**, 909-915, doi:10.1021/ja00082a011 (1994).

25 Lippincott, E. R. & Schroeder, R. One-Dimensional Model of the Hydrogen Bond. *J. Chem. Phys.* **23**, 1099-1106, doi:10.1063/1.1742196 (1955).

26 Staib, A. & Hynes, J. T. Vibrational predissociation in hydrogen-bonded OH···O complexes via OH stretch-OO stretch energy transfer. *Chem. Phys. Lett.* **204**, 197-205, doi:https://doi.org/10.1016/0009-2614(93)85627-Z (1993).

27 McKenzie, R. H., Bekker, C., Athokpam, B. & Ramesh, S. G. Effect of quantum nuclear motion on hydrogen bonding. *J. Chem. Phys.* **140**, 174508, doi:10.1063/1.4873352 (2014).

28 Grabowski, S. J. What Is the Covalency of Hydrogen Bonding? *Chem. Rev.* **111**, 2597-2625, doi:10.1021/cr800346f (2011).

29 Shibata, S. & Bartell, L. S. Electron-Diffraction Study of Water and Heavy Water. *J. Chem. Phys.* **42**, 1147-1151, doi:10.1063/1.1696094 (1965).

30 Ceriotti, M. *et al.* Nuclear Quantum Effects in Water and Aqueous Systems: Experiment, Theory, and Current Challenges. *Chem. Rev.* **116**, 7529-7550, doi:10.1021/acs.chemrev.5b00674 (2016).

31 Weathersby, S. P. *et al.* Mega-electron-volt ultrafast electron diffraction at SLAC National Accelerator Laboratory. *Rev. Sci. Instrum.* **86**, 073702, doi:10.1063/1.4926994 (2015).

32 Bertie, J. E. & Lan, Z. Infrared Intensities of Liquids XX: The Intensity of the OH Stretching Band of Liquid Water Revisited, and the Best Current Values of the Optical Constants of H2O(l) at 25°C between 15,000 and 1 cm-1. *Applied Spectroscopy* **50**, 1047-1057 (1996).

33 Sorenson, J. M., Hura, G., Glaeser, R. M. & Head-Gordon, T. What can x-ray scattering tell us about the radial distribution functions of water? *J. Chem. Phys.* **113**, 9149-9161, doi:Doi 10.1063/1.1319615 (2000).

34 Brockway, L. O. Electron diffraction by gas molecules. *Reviews of Modern Physics* **8**, 0231-0266, doi:DOI 10.1103/RevModPhys.8.231 (1936).

35 Hubbell, J. H. *et al.* Atomic form factors, incoherent scattering functions, and photon scattering cross sections. *J. Phys. Chem. Ref. Data* **4**, 471-538, doi:10.1063/1.555523 (1975).

36 Yang, J. *et al.* Structure retrieval in liquid-phase electron scattering. *arXiv:2006.04234* (2020).

37 Horn, H. W. *et al.* Development of an improved four-site water model for biomolecular simulations: TIP4P-Ew. *J. Chem. Phys.* **120**, 9665-9678, doi:10.1063/1.1683075 (2004).

38 Levine, B. G., Stone, J. E. & Kohlmeyer, A. Fast Analysis of Molecular Dynamics Trajectories with

Graphics Processing Units-Radial Distribution Function Histogramming. *J. Comput. Phys.* **230**, 3556-3569, doi:10.1016/j.jcp.2011.01.048 (2011).

39 Humphrey, W., Dalke, A. & Schulten, K. VMD: Visual molecular dynamics. *Journal of Molecular Graphics* **14**, 33-38, doi:https://doi.org/10.1016/0263-7855(96)00018-5 (1996).

40 Dohn, A. O. *et al.* On the calculation of x-ray scattering signals from pairwise radial distribution functions. *Journal of Physics B-Atomic Molecular and Optical Physics* **48**, 244010, doi:Artn 244010 10.1088/0953-4075/48/24/244010 (2015).

41 Bartell, L. S. & Gavin, R. M. Effects of Electron Correlation in X-Ray and Electron Diffraction. *Journal of the American Chemical Society* **86**, 3493-3498, doi:DOI 10.1021/ja01071a019 (1964).

42 Wang, J. H., Tripathi, A. N. & Smith, V. H. Chemical-Binding and Electron Correlation-Effects in X-Ray and High-Energy Electron-Scattering. *J. Chem. Phys.* **101**, 4842-4854, doi:Doi 10.1063/1.467407 (1994).

43 Hammer, B., Hansen, L. B. & Nørskov, J. K. Improved adsorption energetics within density-functional theory using revised Perdew-Burke-Ernzerhof functionals. *Physical Review B* **59**, 7413-7421, doi:10.1103/PhysRevB.59.7413 (1999).

44 Grimme, S., Antony, J., Ehrlich, S. & Krieg, H. A consistent and accurate ab initio parametrization of density functional dispersion correction (DFT-D) for the 94 elements H-Pu. *J. Chem. Phys.* **132**, 154104, doi:10.1063/1.3382344 (2010).

45 Bussi, G., Donadio, D. & Parrinello, M. Canonical sampling through velocity rescaling. *J. Chem. Phys.* **126**, 014101, doi:10.1063/1.2408420 (2007).

46 Zwanzig, R. in *Non-equilibrium Statistical Mechanics* pp. 18-21 (Oxford University Press: New York, 2001).

47 Ceriotti, M. & Parrinello, M. The δ-thermostat: selective normal-modes excitation by colored-noise Langevin dynamics. *Procedia Computer Science* **1**, 1607-1614, doi:https://doi.org/10.1016/j.procs.2010.04.180 (2010).

48 Marx, D. & Parrinello, M. Ab initio path integral molecular dynamics: Basic ideas. *J. Chem. Phys.* **104**, 4077-4082, doi:10.1063/1.471221 (1996).

49 Cao, J. & Voth, G. A. The formulation of quantum statistical mechanics based on the Feynman path centroid density. III. Phase space formalism and analysis of centroid molecular dynamics. *J. Chem. Phys.* **101**, 6157-6167, doi:10.1063/1.468503 (1994).

50 Markland, T. E. & Ceriotti, M. Nuclear quantum effects enter the mainstream. *Nature Reviews Chemistry* **2**, 0109, doi:10.1038/s41570-017-0109 (2018).

51 Hockney, R. W. & Eastwood, J. W. *Computer simulation using particles.* (Taylor & Francis, Inc., 1988).

52 Plimpton, S. Fast Parallel Algorithms for Short-Range Molecular Dynamics. *J. Comput. Phys.* **117**, 1-19, doi:https://doi.org/10.1006/jcph.1995.1039 (1995).

53 Jr., T. H. D. Gaussian basis sets for use in correlated molecular calculations. I. The atoms boron through neon and hydrogen. *J. Chem. Phys.* **90**, 1007-1023, doi:10.1063/1.456153 (1989).

54 Ufimtsev, I. S. & Martínez, T. J. Quantum Chemistry on Graphical Processing Units. 1. Strategies for Two-Electron Integral Evaluation. *J. Chem. Theory Comput.* **4**, 222-231, doi:10.1021/ct700268q (2008).

55 Ufimtsev, I. S. & Martinez, T. J. Quantum Chemistry on Graphical Processing Units. 2. Direct Self-Consistent-Field Implementation. *J. Chem. Theory Comput.* **5**, 1004-1015, doi:10.1021/ct800526s (2009).

56 Ufimtsev, I. S. & Martinez, T. J. Quantum Chemistry on Graphical Processing Units. 3. Analytical Energy Gradients, Geometry Optimization, and First Principles Molecular Dynamics. *J. Chem. Theory Comput.* **5**, 2619-2628, doi:10.1021/ct9003004 (2009).

57 Yang, J. *et al.* Simultaneous observation of nuclear and electronic dynamics by ultrafast electron diffraction. *Science* **368**, 885-889, doi:10.1126/science.abb2235 (2020).

58 Shibata, S., Sekiyama, H., Tachikawa, K. & Moribe, M. Chemical bonding effect in electron scattering by gaseous molecules. *J. Mol. Struct.* **641**, 1-6, doi:Pii S0022-2860(01)00962-0
Doi 10.1016/S0022-2860(01)00962-0 (2002).

59 Jensen, P. Hamiltonians for the internal dynamics of triatomic molecules. *Journal of the Chemical Society, Faraday Transactions 2: Molecular and Chemical Physics* **84**, 1315-1339, doi:10.1039/F29888401315 (1988).

60 Wilson, E. B. J., Decius, J. C. & Cross, P. C. *Molecular Vibrations: The Theory of Infrared and Raman Vibrational Spectra*. (Dover Publications, 2012).

61 Ceriotti, M., Bussi, G. & Parrinello, M. Colored-Noise Thermostats à la Carte. *J. Chem. Theory Comput.* **6**, 1170-1180, doi:10.1021/ct900563s (2010).

62 Ceriotti, M., Bussi, G. & Parrinello, M. Nuclear Quantum Effects in Solids Using a Colored-Noise Thermostat. *Phys. Rev. Lett.* **103**, 030603, doi:10.1103/PhysRevLett.103.030603 (2009).

63 Marsalek, O. & Markland, T. E. Ab initio molecular dynamics with nuclear quantum effects at classical cost: Ring polymer contraction for density functional theory. *J. Chem. Phys.* **144**, 054112, doi:10.1063/1.4941093 (2016).

64 Habershon, S. & Manolopoulos, D. E. Zero point energy leakage in condensed phase dynamics: An assessment of quantum simulation methods for liquid water. *J. Chem. Phys.* **131**, 244518, doi:10.1063/1.3276109 (2009).

65 Salvat, F., Jablonski, A. & Powell, C. J. ELSEPA - Dirac partial-wave calculation of elastic scattering of electrons and positrons by atoms, positive ions and molecules. *Comput. Phys. Commun.* **165**, 157-190, doi:10.1016/j.cpc.2004.09.006 (2005).

66 Kim, J. G. *et al.* Mapping the emergence of molecular vibrations mediating bond formation. *Nature* **582**, 520-524, doi:10.1038/s41586-020-2417-3 (2020).

67 Császár, A. G. *et al.* First-principles prediction and partial characterization of the vibrational states of water up to dissociation. *J. Quant. Spectrosc. Radiat. Transfer* **111**, 1043-1064, doi:https://doi.org/10.1016/j.jqsrt.2010.02.009 (2010).

68 Soper, A. K. Joint structure refinement of x-ray and neutron diffraction data on disordered materials: application to liquid water. *J. Phys.: Condens. Matter* **19**, 335206, doi:10.1088/0953-8984/19/33/335206 (2007).